Spatial integration effect on velocity spectrum: Towards an interpretation of the –11/3 power law observed in the spectra of turbine outputs

Philippe Druault, Benoît Gaurier, Grégory Germain

Spatial integration effect on velocity spectrum: Towards an interpretation of the $-11/3$ power law observed in the spectra of turbine outputs

Philippe Druault[a,*], Benoît Gaurier[b], Grégory Germain[b]

[a]*Sorbonne Université, CNRS, Institut Jean Le Rond d'Alembert, F-75005 Paris, France*
[b]I FREMER, *Marine Structure Laboratory, 150 quai Gambetta, 62200 Boulogne-sur-mer, France*

Abstract

To improve the turbine operational life, the interaction between flow properties and turbine performance needs to be elucidated. We then propose to examine the physical origin of the power-law scaling in the inertial range of turbine power outputs by experimentally exploring the spectral content of a 1:20 scaled model of a three-bladed horizontal-axis turbine positioned in a 3D turbulent flow. First, measurements confirm that the turbine power frequency spectra exhibit a power law decay proportional to $-11/3$ in the inertial range. Knowing that the turbine power fluctuations are linearly dependent on the incoming velocity fluctuations, PIV measurements are carried out to study the effect of the spatially integrated velocity onto its resulted spectrum. It is demonstrated that in inhomogeneous anisotropic turbulent flow, the velocity spectrum of its spatial average along N direction(s) has an inertial slope of $-5/3 - 2N/3$. This information is used to physically interpret the power-law scaling in the inertial range of the turbine power spectra. The previously observed $f^{-11/3}$ scaling results from a 2D-spatial average velocity field coupled with a spectral average over blades. This physical explanation confirms previous works in which a transfer function was developed between incoming turbulence and the turbine power outputs.

Keywords: wind and tidal turbines, power law decay spectra, power spectral density, turbulence

1. Introduction

Renewable electricity generation from wind and tidal energy has a significant role to play in the transition towards the green energy sources emitting lower

---

*Corresponding author
Email addresses: `philippe.druault@sorbonne-universite.fr` (Philippe Druault), `benoit.gaurier@ifremer.fr` (Benoît Gaurier), `gregory.germain@ifremer.fr` (Grégory Germain)

levels of greenhouse gases. Both wind and tidal-stream are used to convert ki-
netic energy of wind or tidal currents into electricity. To improve the reliability
and the development of these turbines especially by limiting the high operation
and maintenance costs, it is essential to understand the relationship between the
incoming turbulence and the turbine response better. A better knowledge of
the turbine power variabilities related to temporal fine-scale fluctuations could
potentially enable an improvement of the integration of these turbines into the
electricity grid (Lewis et al., 2019; Sentchev et al., 2020). It is now well recog-
nized that turbine performance is mainly impacted by the turbulence intensity
(Mycek et al., 2014; Chamorro et al., 2015c; Li et al., 2016; Blackmore et al.,
2016; Bartl and Sætran, 2017; Ahmed et al., 2017; Durán Medina et al., 2017;
Thiébaut et al., 2020; Allmark et al., 2021; Ebdon et al., 2021) as well as the
mean-shear flow (Bahaj et al., 2007; Wagner et al., 2009; Gaurier et al., 2020a).
Furthermore, the knowledge of the spectral content of turbine outputs is also
necessary to improve the predictability of the produced power, for a better grid
integration of wind or tidal farms (Gayme and Chakrabortty, 2012; Bandi, 2017;
Lewis et al., 2019). Many recent studies are especially focused on the examina-
tion of the turbine power spectrum content (Tobin et al., 2015; Bossuyt et al.,
2017; Deskos et al., 2020).

The nature of the atmospheric turbulent boundary layer flow impacting a
wind turbine is quite similar to the tidal sea-floor boundary layer flow interacting
with a tidal turbine. Indeed, these incoming flows are non-uniform and exhibit
inhomogeneity and anisotropy properties with generally a dominated vertical
mean shear-flow. Moreover, the earth surface roughness and the bathymetric
irregularities of the seafloor generate a complex three dimensional flow field with
possible persistent large scale energetic flow structures (Chamorro et al., 2015a;
Ikhennicheu et al., 2019a). In both cases, the corresponding velocity frequency
spectrum generally exhibits three distinct regions:

1. the first one, in the low-frequency region, is associated with the large scale
   energetic flow structures,
2. the second one corresponds to the inertial range and is related to small
   scale turbulence,
3. the third one, with the highest frequencies, is the dissipative region.

Older works showed the turbine power has a power law slope of $-5/3$ in the
inertial sub-range (Apt, 2007). Recent studies however demonstrate that the
power spectrum of a single wind or tidal turbine located in a turbulent flow
field – satisfying Kolmogorov $-5/3$ power law in the inertial frequency range
(Kolmogorov, 1991) – follows a power law scaling proportional to $-11/3$ (Tobin
et al., 2015; Chamorro et al., 2015a; Liu et al., 2017; Gaurier et al., 2020b).

Tobin et al. (2015) suggest this $-11/3$ power law is linked to the rotational
motion of the blades. Chamorro et al. (2015a) attributes this particular power
law to a turbine which acts as an active low-pass filtering process of the incoming
turbulence. They propose to model this low-pass filtering process by using a
transfer function. The origin of the $f^{-11/3}$ scaling law over the inertial sub-range
is however not yet entirely understood and may still remain questionable.

2

Following the disk average approach for the turbine power of the air-water
flowing through the rotor area, and assuming a constant power coefficient, the
instantaneous power of a single turbine is expressed as follows:

$$P(t) = \frac{1}{2}\rho A \overrightarrow{\mathcal{V}}^3(t) \tag{1}$$

where A is the area swept by the blades and $\overrightarrow{\mathcal{V}}$ indicates the spatial average of
the velocity vector $\overrightarrow{V} = U\overrightarrow{e_x} + V\overrightarrow{e_y} + W\overrightarrow{e_z}$ over A. Generally, the streamwise
velocity component U dominates the other velocity components. Then, applying
the Reynolds decomposition to the instantaneous velocity field (Bossuyt et al.,
2017; Bandi, 2017), the fluctuating part of the turbine power (see section 3.2
for details) can be expressed by:

$$P'(t) \simeq C_1 \overline{\mathcal{U}}^2 \left(\mathcal{U}'(t) + \frac{\mathcal{U}'^2(t)}{\overline{\mathcal{U}}} + \frac{\mathcal{U}'^3(t)}{3\overline{\mathcal{U}^2}} \right) \tag{2}$$

with C_1 a real constant depending on A, and $\mathcal{U}$ is the spatially averaged stream-
wise velocity component. By neglecting higher order terms, the fluctuating part
of the turbine power is then linearly dependent on the fluctuating part of the
spatially integrated velocity field. The turbine power spectrum can not directly
be related to velocity spectrum but to the spectrum of the spatially integrated
(or averaged) velocity fluctuations. In this paper, we propose to investigate the
power law decay of the turbine frequency spectrum by studying the effect of
the spatial average on this spectrum. Similar kind of spatial filtering effects are
furthermore present in many other scientific applications, as presented hereafter.

A one-point measurement of an instantaneous velocity field is rarely obtained
at a single local point but rather along a wire (using Hot Wire Anemometry -
HWA), over a two-dimensional interrogation window (using Particle Image Ve-
locimetry - PIV), over a 2D beam (using Lidar measurements) or over a given
measurement volume (using 3D PIV or Acoustic Doppler Velocimeter - ADV).
The inherent spatial resolution differs then as a function of the measurement
method. This could directly impact the measured velocity spectra (Wyngaard,
1968; Foucaut et al., 2004; Lavoie et al., 2007; Hackett et al., 2009). For instance,
Coherent Doppler Lidar measurements are performed from a laser beam which
is directed along the mean flow direction. It was observed that the effect of the
spatial average (or spatial integration) along the beam onto velocity spectrum
is assimilated to a volume weighting Lorentzian function, corresponding to an
exponential low-pass filter function (Sjöholm et al., 2010). More precisely, the
slopes of the Lidar measurement velocity spectrum are observed to be smaller
than the expected $-5/3$ Kolmogorov's law, in the frequency inertial range. In-
deed, the spatial average process induces a lower spectral kinetic energy within
the inertial range. Globally, it is observed that the velocity spatial average leads
to an attenuation of the spectral energy by filtering the associated small-scale
structures. For PIV measurements, this attenuation is significant and can reach
several times the PIV interrogation window size (Hackett et al., 2009). Sev-
eral 1D or 2D transfer functions are proposed to model this spectral energy

3

reduction, mainly under the Homogeneous Isotropic Turbulence (HIT) flow assumption (Wyngaard, 1968; Lavoie et al., 2007; Hackett et al., 2009). Recently, the effect of the spatial average on velocity measurement is emphasized using a cross-wire probe for inhomogeneous flow field (Baidya et al., 2019).

Another example of the effect of the spatial average on spectra is the power spectral response of a wind farm which is estimated from the spatial average of each individual turbine spectrum. Apt (2007) observes that the spectral slopes of wind power become more negative as the number of interconnected wind turbines increases. Bossuyt et al. (2017) experimentally measure the power from an array of turbines and obtain a higher power law decay in the inertial range. Authors interpret this observation as a consequence of a discrete spatial filter applied on a turbulent boundary layer and derive an associated transfer function. In a similar way, assuming that wind power fluctuations for a single turbine follow the Kolmogorov spectrum of atmospheric turbulence (power law of $-5/3$), Bandi (2017) shows that the power spectral response of a farm composed of a high number of turbines has an asymptotic power law decay of $-7/3$. This result is in accordance with the work of Katzenstein et al. (2010) which shows that the power spectrum computed from a plant of 20 wind turbines is proportional to $f^{-2.56} \simeq f^{-7/3}$. To demonstrate the asymptotic limit of $f^{-7/3}$ on the spatial average velocity spectra, Paraz and Bandi (2019) analyze the effect of a spatial filter onto the velocity spectra of a HIT turbulence satisfying the Kolmogorov's law of $-5/3$ in the inertial range. Based on experimental database, they show the spatial average effect onto a velocity spectrum results in an exponential convergence of the spectral power law towards $-7/3$ as the number of velocity signals increases. These previous works deal with homogeneous and isotropic temporal velocity signals.

As high-Reynolds number turbulent flow is generally anisotropic and presents mean-shear profile, the purpose of this paper is then to obtain a general answer for the effect of the spatial average (which can similarly be viewed as spatial integration) on the velocity spectrum of such a turbulent flow field. This should constitute a new interesting way to analyze and interpret the spectral properties of a single turbine power output. For such an investigation, the wake flow developing behind a wall-mounted square cylinder is experimentally considered. Such a inhomogeneous anisotropic flow presents a mean vertical shear and some large scale energetic structures. Such a wake profile has a significant anisotropic effect that can be related to atmospheric boundary layer flow. Note that the present wake flow configuration is also of interest because it enables similar flow conditions to be reproduced, as when a turbine is located in the wake of an upstream turbine (Churchfield et al., 2012). In this work, a single turbine is successively positioned at different streamwise locations in the wake of a wall-mounted square cylinder and the power turbine spectral output is measured. Its theoretical link to a spatial average velocity field is then established.

After a description of the experimental set-up and the used databases, the turbine thrust force and torque momentum are processed to compute their associated power spectral densities. PIV planar measurements are then analyzed showing the effect of the spatial average on the velocity frequency spectrum.

4

Finally, after commenting these effects, a physical interpretation of the $-11/3$ power slope of the power spectrum produced by the turbine is provided.

2. Description of the databases

2.1. Experimental set-up

The tests are carried out in the wave and current circulating flume tank of IFREMER with a test section of 18 m long × 4 m wide × 2 m deep (Gaurier et al., 2018). The experimental set-up consists of a wall bottom-mounted cylinder and, in its wake, a tri-bladed horizontal axis tidal turbine, both at a one to twenty scale (figure 1). The scaled experiment corresponds to real sea conditions of a tidal site (Ikhennicheu et al., 2019b). The square wall-mounted cylinder has an aspect ratio $AR = W/H = 6$, with W the width and $H = 0.25\,\mathrm{m}$ the height of the cylinder. The instrumented scale turbine has a diameter $D = 0.72\,\mathrm{m}$.
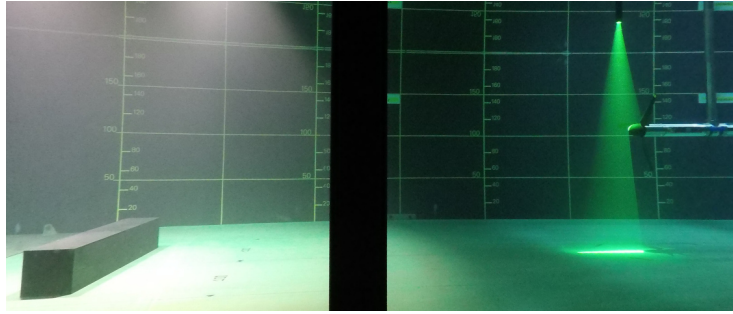

Figure 1: Experimental set-up including the wall-mounted cylinder, the horizontal-axis turbine model and the PIV laser sheet in front of the rotor.

The incoming flow $(U_\infty, V_\infty, W_\infty)$ is assumed to be steady and uniform, with $U_\infty = 1\,\mathrm{m\,s^{-1}}$ and $V_\infty = W_\infty = 0$. The three instantaneous velocity components are denoted (U, V, W) along the (x, y, z) directions respectively. The Reynolds decomposition applying to the streamwise velocity component leads to $U(\mathbf{X}, t) = \overline{U(\mathbf{X})} + u'(\mathbf{X}, t)$ where the overline indicates the time average. A low turbulent intensity $I_\infty = 1.5\,\%$ is imposed at inlet. In the following, spatial variables (x, y, z) are normalized with H and the corresponding notations are used: $x^* = x/H$, $y^* = y/H$ and $z^* = z/H$.

For the present investigation, the incoming flow Reynolds number is:

$$Re = \frac{HU_\infty}{\nu} = 2.5 \times 10^5 \tag{3}$$

with ν the water kinematic viscosity. The Froude number is:

$$Fr = \frac{U_\infty}{\sqrt{gD_e}} = 0.23 \tag{4}$$

5

with D_e the flume tank depth and g the gravity.

The instrumented turbine used in this study includes thrust, torque and blade root load measurements (figures 2a and 2b). The blades (with a fixed pitch angle) are made of moulded carbon fibre reinforced plastic and are based on a NACA 63-418 profile, see Gaurier et al. (2015) for a detailed geometry. The root of each blade is instrumented with a load transducer measuring forces in the flapwise and edgewise directions: F_{xi} along e_x (contributing to the thrust T) and F_{yi} along e_y (contributing to the torque Q) for blade i and bending moments along the three orthogonal directions (e_x, e_y and e_z). These 5 loads per blade are all integrated along the rotating blade length. Thrust T and torque Q experienced by the rotor are also measured separately by a torque and thrust transducer. The load instrumentation is located upstream of the shaft seal to prevent the measurements being affected by the friction associated with the seal. The transducers are therefore made waterproof. The turbine model generator is animated by a permanent magnet brushed motor fitted with a 1:26 ratio gearbox.

(a) the turbine model   (b) schematic of the load transducer
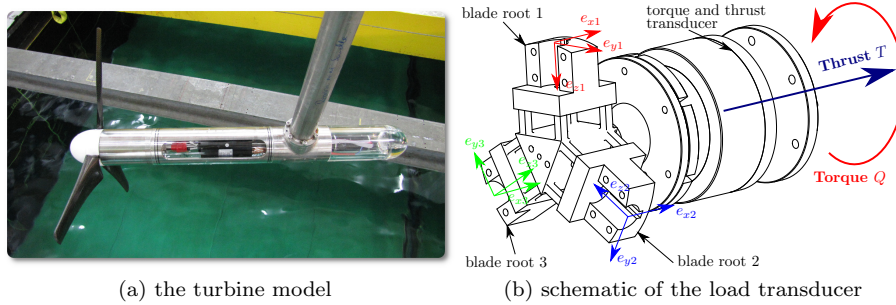
Figure 2: Horizontal-axis turbine model used in the experiments with a detailed schematic of the waterproof transducers measuring the blade root loads and the rotor thrust and torque.

For this work, the turbine is used at its nominal functionning point i.e. the design Tip Speed Ratio corresponding to $TSR = 4$ (Magnier et al., 2020) and positioned at mid-depth in the tank. Four successively streamwise locations downstream to the wall-mounted cylinder, corresponding to $x^* = [4; 10; 16; 23]$, are considered.

2.2. Presentation of the databases

In order to give a physical interpretation of the $-11/3$ power slope of the spectrum of the power produced by the turbine, three databases are used. The first and main one implements the entire experimental device (wall-mounted cylinder and turbine model) with Particle Image Velocimetry (PIV) measurements in front of the turbine rotor, coupled with the torque momentum and thrust force measurements (database A). The two other databases (B and C) are only flow measurements (without the turbine) used in order to characterize the velocity variations encountered in the wake of the wall-mounted cylinder

Database	Measurement	Plane Orientation	Discretization [pixel]	Meshgrid $(N_x \times N_y)$ or $(N_x \times N_z)$	Spatial Discretization	Sampling Frequency and Duration
A	PIV	Vertical	330×840	30×74	$11.2\,\mathrm{mm}$	$15\,\mathrm{Hz}$ - $180\,\mathrm{s}$
	Thrust/Torque	Turbine	-	-	-	$120\,\mathrm{Hz}$ - $180\,\mathrm{s}$
B	PIV	vertical	1600×600	99×36	$11.6\,\mathrm{mm}$	$15\,\mathrm{Hz}$ - $150\,\mathrm{s}$
C	PIV	horizontal	1600×1200	99×74	4.8 to $7.1\,\mathrm{mm}$	$15\mathrm{Hz}$ - $150\,\mathrm{s}$

Table 1: Experimental set-up parameters of each database

and to analyze the spatial integration effect on the velocity spectrum. Vertical measurement planes of database B are required to investigate the spatial averaging effect along both x and z directions onto velocity spectra, while horizontal measurement planes of database C are required to investigate the spatial averaging effect along both x and y directions. Figure 3 and table 1 display and contain the main information about the number and the location of the PIV measurement planes of each database. The reader is referred to previous cited works for details about experimental set-up, the measurement method implementation, the acquisition parameters and the associated measurement error. The main characteristics of the three databases are the following ones:

1. database A (Gaurier et al., 2020a,b): one vertical PIV measurement plane (x, z) located just in front of the operating turbine. The PIV plane is centered vertically at hub height and ends horizontally at the blade root. These PIV measurements have also been repeated at the same position without the turbine. Due to shadowing effect in the measurement plane, only the instantaneous velocity field extracted along a vertical line at the x-centered plane position is retained for analysis.

2. database B (Ikhennicheu et al., 2019b): 5 vertical PIV measurement planes (x, z) along the transverse symmetrical axis $(y = 0)$. The (x^*, z^*) range positions of each plane are detailed in table 2.

3. database C (present work): 5 horizontal PIV measurement planes (x, y) along the z direction. These planes are located in the far field at different heights from $z^* = 3$ to $z^* = 5$ (see table 3) in and out the wall-mounted cylinder wake.
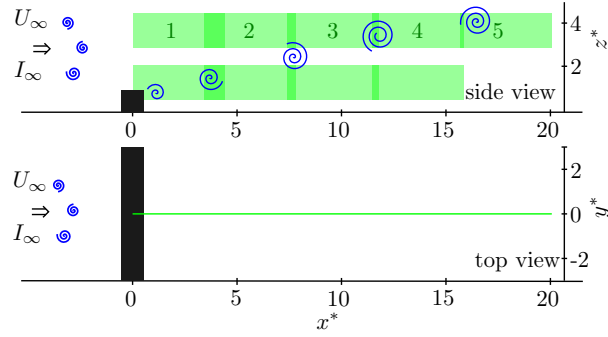
Previous investigations (Ikhennicheu et al., 2019b) have shown that the cylinder wake flow exhibits large scale flow structures corresponding to a Strouhal number:
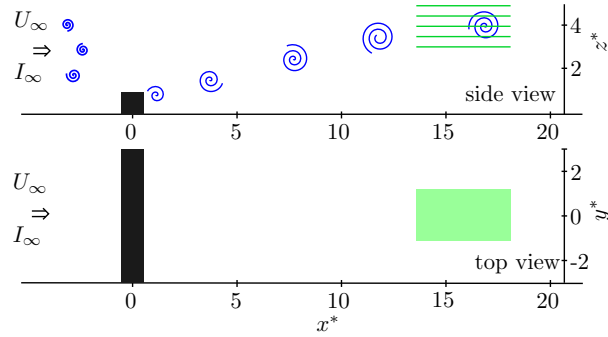
$$St = \frac{fH}{U_\infty} = 0.07 \tag{5}$$

This Strouhal number corresponds to a structure frequency passage of $f = 0.28\,\mathrm{Hz}$. Each PIV dataset spans more than 40 large eddy turnover times, as-
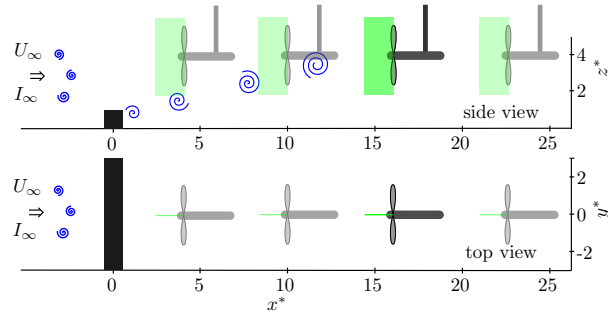
(a) Database A

(b) Database B

(c) Database C

Figure 3: Schematic views of the experimental set-up showing the location of the PIV measurement planes (green rectangles). Database A: vertical PIV measurements with/without the synchronized acquisition of the turbine parameters and the four successive rotor locations $x^* = [4; 10; 16; 23]$. The location $x^* = 16$ is highlighted. Database B: vertical PIV measurements in the wake of the wall-mounted cylinder with plans 1 to 5 considered in this study for the spectral analysis. Database C: horizontal PIV measurements in the wake of the wall-mounted cylinder.

y^* position	x^* extend	z^* extend	Spatial Discretization
0	$[-0.2:4.4]$	$[2.6:4,3]$	$11.6\,\mathrm{mm}$
0	$[3.3:7.9]$	$[2.6:4,3]$	$11.6\,\mathrm{mm}$
0	$[7.4:12.0]$	$[2.6:4,3]$	$11.6\,\mathrm{mm}$
0	$[11.0:15.6]$	$[2.6:4,3]$	$11.6\,\mathrm{mm}$
0	$[15.3:19.9]$	$[2.6:4,3]$	$11.6\,\mathrm{mm}$

Table 2: Database B: details of the locations of the 5 vertical PIV measurement planes.

z^* position	x^* extend	y^* extend	Spatial Discretization
3.0	$[14.67:16.57]$	$[-0.60:0.81]$	$4.8\,\mathrm{mm}$
3.5	$[14.61:16.67]$	$[-0.66:0.88]$	$5.3\,\mathrm{mm}$
4.0	$[14.44:16.84]$	$[-0.78:1.00]$	$6.1\,\mathrm{mm}$
4.5	$[14.39:16.90]$	$[-0.82:1.05]$	$6.4\,\mathrm{mm}$
5.5	$[14.26:17.03]$	$[-0.92:1.15]$	$7.1\,\mathrm{mm}$

Table 3: Database C: details of the locations of the 5 horizontal PIV measurement planes

suring the statistical convergence of the data. On the other hand, the streamwise integral time scale is computed. It is defined as follows:

$$T_x = \int_0^\infty \frac{\overline{u'(t)u'(t+\tau)}}{\overline{u'^2}} d\tau \tag{6}$$

with $\overline{u'(t)u'(t+\tau)}/\overline{u'^2}$ representing the temporal streamwise time auto-correlation. In the far wake, this auto-correlation is estimated at a fixed streamwise location $x^* \simeq 19$ and for several z positions: $z^* \in [3.5;5]$, from database C (see figure 4). Using the overall average value (black line in the figure), the integral time scale T_x can be computed by integrating the temporal auto-correlation in time until it crosses zero for the first time ($\tau \simeq 1\,\mathrm{s}$). Using Taylor hypothesis with $U_\infty = 1\,\mathrm{m\,s^{-1}}$ under frozen turbulence assumption, the integral length scale is found to be of $L_x = 0.40\,\mathrm{m}$. This length scale is smaller than the rotor diameter ($D = 0.72\,\mathrm{m}$). Besides, the Kolmogorov length scale based on the isotropic dissipation rate was previously estimated thanks to Laser Doppler Velocimetry (Ikhennicheu et al., 2020). This scale approaches $0.07\,\mathrm{mm}$ which is much smaller than the PIV meshgrid, of $\Delta_{piv} \simeq 11\,\mathrm{mm}$.

Note that in the present flow configuration, the integral length-scale is always smaller than the rotor diameter. In real in-situ conditions, this may not be always the case and the integral flow lenght-scale and its relation with the rotor diameter, will certainly influence the small scale filtering process. For this reason, in the following spectra plots, we will indicate the frequency corresponding to the integral time-scale. This frequency is determined from the average value of the integral time-scale (figure 4) calculated along z direction at the x-centered plane position of each PIV measurement plane (database A and B).
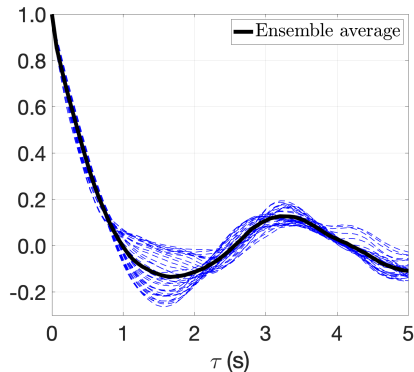
Figure 4: Temporal auto-correlations of the streamwise velocity component $\overline{u'(t)u'(t+\tau)}/\overline{u'^2}$, determined at a fixed x position $x^* = 19$ for several z positions $z^* \in [3;5]$ (database C). Black line indicates the ensemble average over each available z-temporal correlation.

Spectral analyses have been previously conducted from high resolved LDV measurements and results are compared to those determined from present PIV database B. It is shown that the inertial sub-range is well reproduced from
245 PIV database (Ikhennicheu, 2019). The sample rate (15 Hz) and the length of the time velocity signals (superior or equal to 150 s) then enable to both the energy-containing scale and the inertial range scale to be accessed.

These remarks emphasize that the present PIV sampling strategy does not enable all space and time flow scales to be extracted, especially the dissipa-
250 tive scales. However, even if the dissipation range is not reached in spectral representation, the inertial range under interest is well accessed.

2.3. Mean flow characterization

Figure 5 displays $\overline{U}$ measured in front of the rotating turbine and with no turbine at the same four x-positions, from database A. The vertical mean shear
255 flow is confirmed and this representation emphasizes that the rotating turbine notably modifies the shear of the mean flow, especially due to the presence of the hub. This shear modification is expected to be similar as well along the spanwise y-direction. The mean velocity profiles are not exactly symmetric about the hub. This is due to the incoming asymmetric shear flow generating
260 skewed fluctuations.

Figure 6 presents the mean streamwise velocity component along the symmetrical axis $y = 0$, from database B. Above the black line (materializing $\overline{U} = 0.9U_\infty$), the mean flow is accelerated until $x^* > 2.5$ and then the magnitude of $\overline{U}$ decreases as the distance to the cylinder increases. A vertical mean shear
265 flow is clearly observed and this shear flow is also present in other transverse planes ($y^* = 1$ and $y^* = 2$) as shown by Ikhennicheu et al. (2019b).

Figure 7 displays two illustrative mean streamwise velocity maps in far downstream (x, y) planes: $z^* = 3.5$ (figure 7a) and $z^* = 5$ (figure 7b) from database
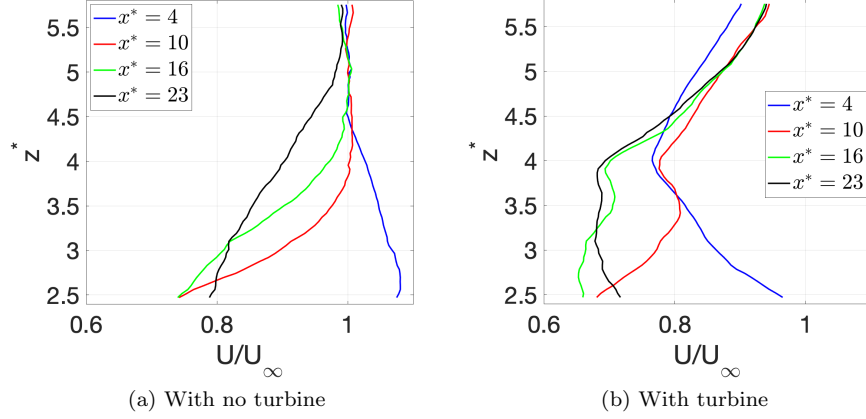
10

(a) With no turbine

(b) With turbine

Figure 5: Database A result: mean streamwise velocity component along a vertical z-line at the four x positions (Database A) with no turbine and in presence of the rotating turbine at $TSR = 4$.
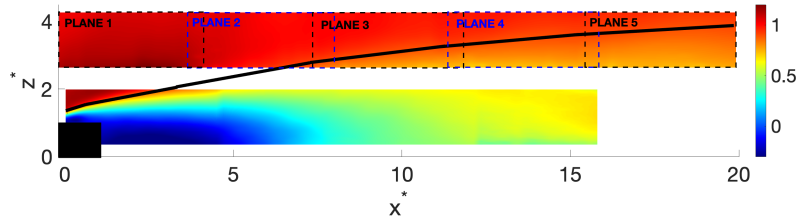

Figure 6: Database B result: mean streamwise velocity component in the symmetrical $y = 0$ plane (database B). Black line indicates the location where $\overline{U} = 0.9U\infty$. Dotted lines indicate the 5 PIV measurement planes.

C. As previously shown, these two planes are located inside and outside the wake region respectively. Outside the wake region where the flow is uniform (figure 7b), the streamwise mean velocity component is homogeneous along y direction. However, some small variabilities in the wake region are still present (figure 7a). A very small mean shear flow is also observed along the x direction.

Previous representations emphasize the inhomogeneous flow field, particularly with a high vertical shear. This shear is modified by the presence of the turbine as well. Previous studies were mainly focused on the spatial averaging effect along the homogeneous flow direction onto the resulting velocity frequency
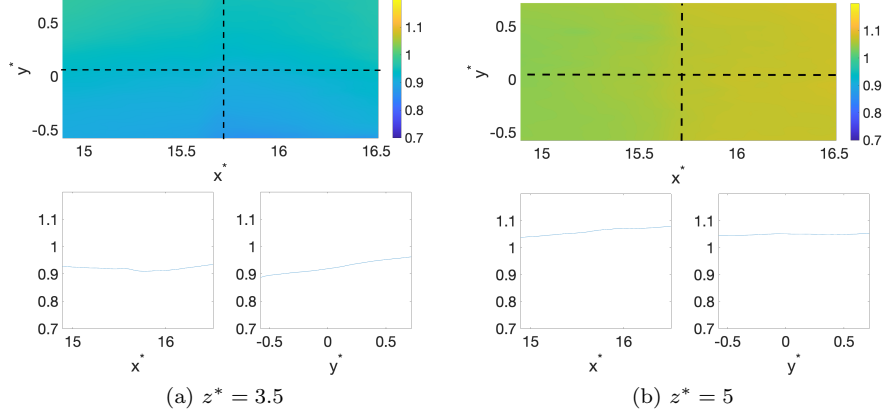
11

Figure 7: Database C result: measurement plane located at $z^* = 3.5$ and $z^* = 5$. Mean streamwise velocity component in (x,y) plane (top) and along the x centerline (bottom left) along the y centerline (right left).

spectra, the present flow field seems a good candidate to investigate this effect in presence of a shear flow field.

3. Spectra of the turbine torque momentum and thrust force

The thrust force and torque momentum measurements are firstly analyzed in the spectral Fourier domain. Secondly, the theoretical link between turbine power or force fluctuations and incoming fluctuating velocities are derived.

3.1. Spectral analysis of the thrust and torque

The turbine thrust T and torque Q fluctuations of the turbine model under specific turbulent shear flow conditions are investigated in the frequency domain for four turbine locations: $x^* = [4; 10; 16; 23]$ (database A). The spectral analysis is conducted from available signals sampled at the frequency $f_s = 120$ Hz, for a duration of 180 s (see table 1). To enhance the Discrete Fourier Transform computation, each signal is separated into N blocks of 2^{11} samples overlapping with 50 %. The Power Spectral Densities (PSD) are represented in a logarithmic plot on figure 8. It is remarkable that whatever the incoming flow conditions (i.e. whatever the x-position), the PSD show similar trends:

1. a low-frequency peak (between 0.2 and 0.3 Hz) associated with the periodic passage of the large scale flow structures in the cylinder wake;
2. two main peaks ($\simeq 5.4$ Hz and $\simeq 10.8$ Hz) corresponding to three times the rotation frequency of the turbine and its first harmonic. The main peak of the PSD is located at $3 \times f_r = 5.4$ Hz, i.e. the blade passing frequency. These energy peaks around the blade passing frequency have also been previously highlighted by Chamorro et al. (2013); Payne et al. (2018).

12

3. a power law in the inertial sub-range, proportional to $-11/3$. These results are in accordance with previous works, e.g. Tobin et al. (2015); Chamorro et al. (2015b); Liu et al. (2017); Gaurier et al. (2020b); Jin et al. (2016).
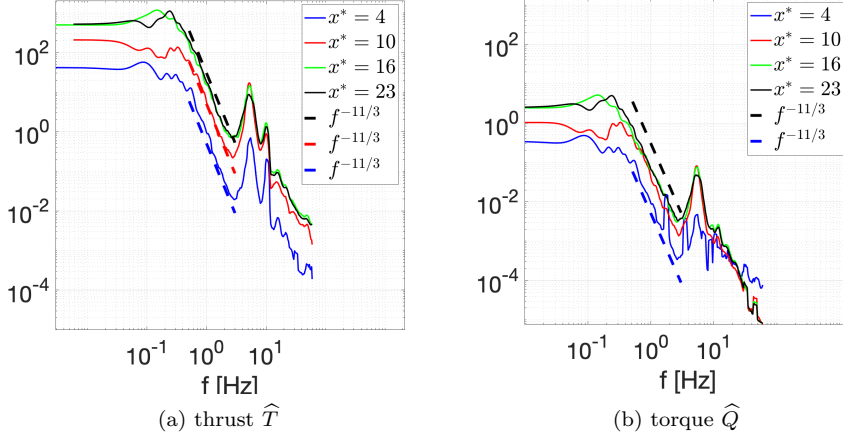

(a) thrust $\widehat{T}$

(b) torque $\widehat{Q}$

Figure 8: Superimposition of the Power Spectral Densities (PSD) of the turbine thrust (T) and torque (Q) fluctuations, processed at each x-position (database A). Dashed lines indicate the power law: $f^{-11/3}$.

3.2. Turbine thrust and power analytical expression

305   Following the disk average of the flow going through the turbine rotor area, the power P and thrust T parameters are generally expressed as follows:

$$T = \frac{1}{2}\rho A C_T V_0^2 \tag{7}$$

$$P = \frac{1}{2}\rho A C_P V_0^3 = Q \times \Omega \tag{8}$$

where A is the turbine swept area and (C_P, C_T) are the coefficients of power and of thrust respectively. As the choice of a reference velocity V_0 in a shear flow still remains ambiguous, we first use the disk average reference velocity, like proposed by Bossuyt et al. (2017); Bandi (2017). If coefficients (C_P, C_T) are assumed to be constant, the instantaneous performance-related parameters are:

$$P(t) \simeq K_1 \overrightarrow{\mathcal{V}}^3(t) \tag{9}$$

$$T(t) \simeq K_2 \overrightarrow{\mathcal{V}}^2(t) \tag{10}$$

315   where (K_1, K_2) are two real constants and $\overrightarrow{\mathcal{V}}(t)$ is the spatial integration (or average) over the rotor area of the instantaneous velocity field. The streamwise component dominates the other components of the velocity and previous

13

expressions become: $P(t) \simeq K_1\mathcal{U}^3(t)$ and $T(t) \simeq K_2\mathcal{U}^2(t)$. After decomposing the spatially averaged velocity field in a temporal mean and fluctuating parts: $\mathcal{U}(t) = \overline{\mathcal{U}} + \mathcal{U}'(t)$ with $\overline{\mathcal{U}'} = 0$, equations 10 and 9 respectively become:

$$P(t) \simeq K_1\left(\overline{\mathcal{U}}^3 + 3\,\overline{\mathcal{U}}^2\mathcal{U}'(t) + 3\,\overline{\mathcal{U}}\mathcal{U}'^2(t) + \mathcal{U}'^3(t)\right) \tag{11}$$

$$T(t) \simeq K_2\left(\overline{\mathcal{U}}^2 + 2\,\overline{\mathcal{U}}\mathcal{U}'(t) + \mathcal{U}'^2(t)\right) \tag{12}$$

Only keeping the time average of each equation, the mean and fluctuating part of these two quantities are expressed as follows:

$$\begin{cases} \overline{P} \simeq K_1\left(\overline{\mathcal{U}}^3 + 3\,\overline{\mathcal{U}\mathcal{U}'^2} + \overline{\mathcal{U}'^3}\right) \\ \overline{T} \simeq K_2\left(\overline{\mathcal{U}}^2 + \overline{\mathcal{U}'^2}\right) \end{cases} \tag{13}$$

and

$$\begin{cases} P'(t) \simeq 3K_1\overline{\mathcal{U}}^2\left(\mathcal{U}'(t) + \dfrac{\mathcal{U}'^2(t)}{\overline{\mathcal{U}}} + \dfrac{\mathcal{U}'^3(t)}{3\,\overline{\mathcal{U}}^2}\right) \\ T'(t) \simeq 2K_2\overline{\mathcal{U}}\left(\mathcal{U}'(t) + \dfrac{\mathcal{U}'^2(t)}{2\,\overline{\mathcal{U}}}\right) \end{cases} \tag{14}$$

As the contribution of high order terms is negligible as a first approximation (Bossuyt et al., 2017), the fluctuating parts of the turbine power and thrust are then linearly dependent on the fluctuating part of the spatially averaged velocity field:

$$\begin{cases} P'(t) \simeq 3K_1\,\overline{\mathcal{U}}^2\mathcal{U}'(t) \\ T'(t) \simeq 2K_2\,\overline{\mathcal{U}}\mathcal{U}'(t) \end{cases} \tag{15}$$

As a disk-average assumption can be unsatisfactory or experimentally difficult to quantify, new thrust and power expressions are proposed. The instantaneous thrust and power fluctuations are now viewed as the instantaneous F_{xi} and F_{yi} contribution over the three turbine blades i (see schematic 2b), at each instant. Based on similar assumptions, a more realistic expression of turbine performance parameters is proposed:

$$\begin{cases} P = \displaystyle\sum_{i=1}^{3} \frac{1}{2}\rho A_{blade}C_P\mathcal{U}_i(t)^3 \\ T = \displaystyle\sum_{i=1}^{3} \frac{1}{2}\rho A_{blade}C_T\mathcal{U}_i(t)^2 \end{cases} \tag{16}$$

where A_{blade} is the blade area and $\mathcal{U}_i$ corresponds to the weighted i^{th} blade-averaged area of the streamwise velocity component.

Similarly to above, the fluctuating parts of the turbine power and thrust could also be expressed as follows:

$$\begin{cases} P'(t) \simeq K_3\displaystyle\sum_{i=1}^{3}\mathcal{U}_i'(t) \\ T'(t) \simeq K_4\displaystyle\sum_{i=1}^{3}\mathcal{U}_i'(t) \end{cases} \tag{17}$$

14

where (K_3, K_4) are two real constants depending on $\overline{\mathcal{U}_i}$, A_{blade} and (C_P, C_T) respectively. Equations 17 demonstrate that the thrust and power fluctuations arise from the spatially integrated velocity variabilities. The spectral content of these parameters measuring the turbine performance is then directly linked to the spectral content of spatially averaged (or integrated) velocity field:

$$
\begin{cases}
\widehat{P'}(f) \simeq K_3 \widehat{\sum_{i=1}^{3} \mathcal{U}_i'}(f) \\
\widehat{T'}(f) \simeq K_4 \widehat{\sum_{i=1}^{3} \mathcal{U}_i'}(f)
\end{cases}
\tag{18}
$$

The purpose of this work is then to address the effect of such spatial average – and especially the inertial range behaviour – on the resulted velocity spectrum. The final aim is to propose an interpretation of the inertial range power-law exponent of the PSD regularly observed on the turbine-performance parameters.

4. Spatial averaging effect on velocity frequency spectra

As detailed in section 2.3, the flow mainly presents a mean vertical shear (z-direction) and inhomogeneous properties along the x-direction due to the rising development of the cylinder wake. On the contrary, the flow shows homogeneous characteristics along the spanwise y-direction. These properties are studied in this section from a spectral point of view, focusing on the power-low processed from various spatial averaging operations of the velocity. Only the streamwise velocity component is considered for this investigation. The instantaneous spatial average of the streamwise velocity component is denoted $\mathcal{U}(t)$. The three 2D planar PIV velocity databases (see section 2.2) are used to successively investigate the effect of the spatial average over one direction (x, y or z) and over two dimensions ((x, y) or (x, z)). Each velocity signal is sampled at a frequency $fe = 15\,\mathrm{Hz}$ and for a duration of $150\,\mathrm{s}$ or $180\,\mathrm{s}$ (see table 1). The following spectral notation is used:

1. $\widehat{\mathcal{U}}_d$ where $d = x$, y or z stands for the spectra of the 1D-spatial average velocity computed along the corresponding direction,
2. $\widehat{\mathcal{U}}_{xy}$ and $\widehat{\mathcal{U}}_{xz}$ correspond to the spectra of the 2D-spatial average velocity computed along both x, y-directions and x, z-directions respectively.

All the PSD shown in this section are processed following the same procedure: each signal is separated into blocks of 1024 samples overlapping with 50 %.

4.1. Description of the spatial averaging methods

Several spatial averaging methods have been applied to the velocity signal before processing the PSD. Planar PIV databases obtained in y plane (database B) and in z plane (database C) are firstly considered to calculate both 1D and 2D spatial averaging effect. Figure 9 presents the two methods used to determine $\mathcal{U}(t)$ for database C. The same procedure is applied for database B, with a different plane size and a different orientation: the z-axis replaces the y-axis comparing to database C.

15

(a) 1D-spatial averaging along x or y direction
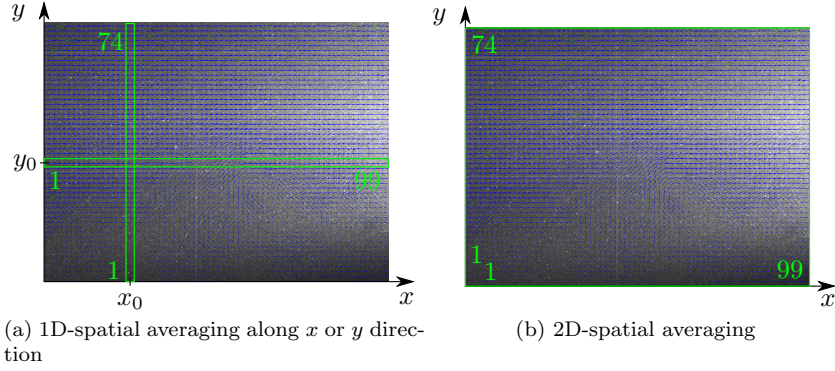
(b) 2D-spatial averaging

Figure 9: Schematic of the 1D and 2D spatial averaging methods used for database C.

In each measurement (x, y)-plane and according to the schematic 9a, the following 1D-spatial averaging velocities are computed:

$$
\begin{cases}
\mathcal{U}_y(t) = \dfrac{1}{N_y} \displaystyle\sum_{iy=1}^{N_y} U(x_0, iy, t) \\
\mathcal{U}_x(t) = \dfrac{1}{N_x} \displaystyle\sum_{ix=1}^{N_x} U(ix, y_0, t)
\end{cases}
\tag{19}
$$

where (N_x, N_y) are the number of meshgrid points in PIV measurement plane, i.e. $(N_x, N_y) = (99, 74)$ for database C (see table 1), and for fixed x_0 and y_0
380 positions. $U(x_0, iy, t)$ and $U(ix, y_0, t)$ are the instantaneous streamwise velocity components, at the Eulerian (x_0, iy) and (ix, y_0) points respectively.

With the same procedure, the following expressions are determined for database B in a (x, z)-plane:

$$
\begin{cases}
\mathcal{U}_z(t) = \dfrac{1}{N_z} \displaystyle\sum_{iz=1}^{N_z} U(x_0, iz, t) \\
\mathcal{U}_x(t) = \dfrac{1}{N_x} \displaystyle\sum_{ix=1}^{N_x} U(ix, z_0, t)
\end{cases}
\tag{20}
$$

with $(N_x, N_z) = (99, 36)$ (see table 1) for fixed x_0 and z_0 positions.

385 In the same way and according to figure 9b, the 2D-spatial average velocities are expressed by the following formula for database C and B respectively:

$$
\begin{cases}
\mathcal{U}_{xy}(t) = \dfrac{1}{N_x N y} \displaystyle\sum_{ix=1}^{N_x} \sum_{iy=1}^{N_y} U(ix, iy, t) \\
\mathcal{U}_{xz}(t) = \dfrac{1}{N_x N_z} \displaystyle\sum_{ix=1}^{N_x} \sum_{iz=1}^{N_z} U(ix, iz, t)
\end{cases}
\tag{21}
$$

16

Because the plane size recorded for database A is mainly vertical, we choose these corresponding recorded velocities for a deeper analysis applied on the 1D-spatial averaging only. The influence of the number of Eulerian points composing the 1D-spatial averaging velocity is tested. For each acquisition case, the streamwise velocity component is instantaneously available for $N_z = 74$ Eulerian points, covering the entire diameter of the turbine (see figure 10).
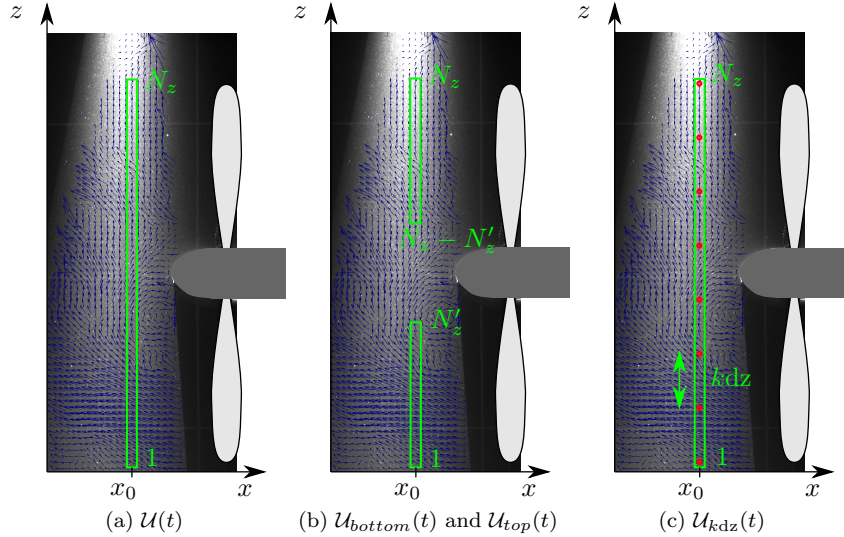

Figure 10: Schematic of the 1D-spatial averaging methods applied on the results coming from database A, with and without the turbine. $\mathcal{U}(t)$ is averaged on the entire turbine diameter or divided into two different parts: $\mathcal{U}_{bottom}$ and $\mathcal{U}_{top}$ with a varying N'_z value or finally processed with a varying discretization step $k$dz.

According to figure 10a, the 1D-spatial averaging velocity upstream to the turbine rotor is expressed with:

$$\mathcal{U}(t) = \frac{1}{N_z} \sum_{iz=1}^{N_z} U(iz, t) \tag{22}$$

with $N_z = 74$ points. This signal is based on all available uniformly distributed Eulerian points covering the turbine diameter.

Varying the number of Eulerian points in the $\mathcal{U}(t)$ signal, we introduce the N'_z value defining two new averaged velocities: $\mathcal{U}_{top}(t)$ and $\mathcal{U}_{bottom}(t)$ (figure 10b). These two 1D-spatial averaging velocities are defined with the following formula:

$$
\begin{cases}
\mathcal{U}_{top}(t) = \dfrac{1}{N'_z} \displaystyle\sum_{iz=N_z-N'_z}^{N_z} U(iz, t) \\[2ex]
\mathcal{U}_{bottom}(t) = \dfrac{1}{N'_z} \displaystyle\sum_{iz=1}^{N'_z} U(iz, t)
\end{cases} \tag{23}
$$

17

$\mathcal{U}_{top}(t)$ and $\mathcal{U}_{bottom}(t)$ both contain N'_z Eulerian points, which is always lower or equal to N_z.

The effect of the spatial discretization step between two consecutive Eulerian points is analyzed as well. The physical distance between two consecutive raw velocity signals is $dz = 11.6\,\text{mm}$. A third 1D-spatial averaging velocity is then introduced depending on a step $k\text{dz}$ leading to:

$$\mathcal{U}_{k\text{dz}}(t) = \sum_{iz} U(iz, t) \tag{24}$$

with iz varying between 1 and N_z, with a step $k\text{dz}$ as depicted on figure 10c.

4.2. 1D and 2D spatial averaging effects

Whatever (x_0, z_0), the spectra $\widehat{\mathcal{U}}_z(x_0, f)$ and $\widehat{\mathcal{U}}_x(z_0, f)$ obtained from 1D-spatial averaging velocities show similar trends for database B. Some illustrative PSD examples are displayed on figure 11 with green and red curves, where (x_0, z_0) is located near the center of each plane. A one-point velocity PSD satisfying the Kolmogorov's $-5/3$ power law decay is also plotted for comparison (blue curve). An inertial range power law exponent of $-7/3$ is obtained for each measurement plane and for $\widehat{\mathcal{U}}_z$ or $\widehat{\mathcal{U}}_x$. Similar observations are observed for database C (figure 12). The effect of spatial filtering is clearly noticed with a lower energy in the inertial range. This is in accordance with previous studies showing that the spatial averaging acts as an energetic filtering in the inertial sub-range (Wyngaard, 1968; Lavoie et al., 2007; Hackett et al., 2009). The most interesting observation is the $-7/3$ scaling exponent in the sub-range, which differs from the Kolmogorov's exponent observed for the one-point velocity PSD (blue curves). Whatever the location in the wake flow and the direction along which the spatial average is conducted, each spectrum exhibits this same power law decay in the inertial range. This result can be related to previous work dealing with the effect of spatial averaging in a HIT turbulent flow (Paraz and Bandi, 2019). By comparison with these previous studies, each PSD of the 1D-spatial averaging velocity converges towards a $-7/3$ scaling in the inertial range, even if the number of Eulerian points is lower ($N_z = 36$ only for database B). A detailed analysis of the power law exponent convergence is presented in section 4.3.

PSD obtained from the 2D-spatial averaging velocity are presented as well on figures 11 and 12 with black curves. According to these results, when the spatial averaging is performed along two directions (either (x, y) or (x, z)), the resulted spectra follow a power law decay of -3 in the inertial sub-range. This is especially the case of the $\widehat{\mathcal{U}}_{xz}$ spectrum (figure 11) due to the fact that a high shear flow direction (z one) increases the convergence, as discussed in the next section. $\widehat{\mathcal{U}}_{xy}$ also presents such a power law decay (figure 12) but this result suffers from a poor convergence due to small number of points and poor flow dynamics, especially for $z^* > 4$ (outside the wake, figure 12b).
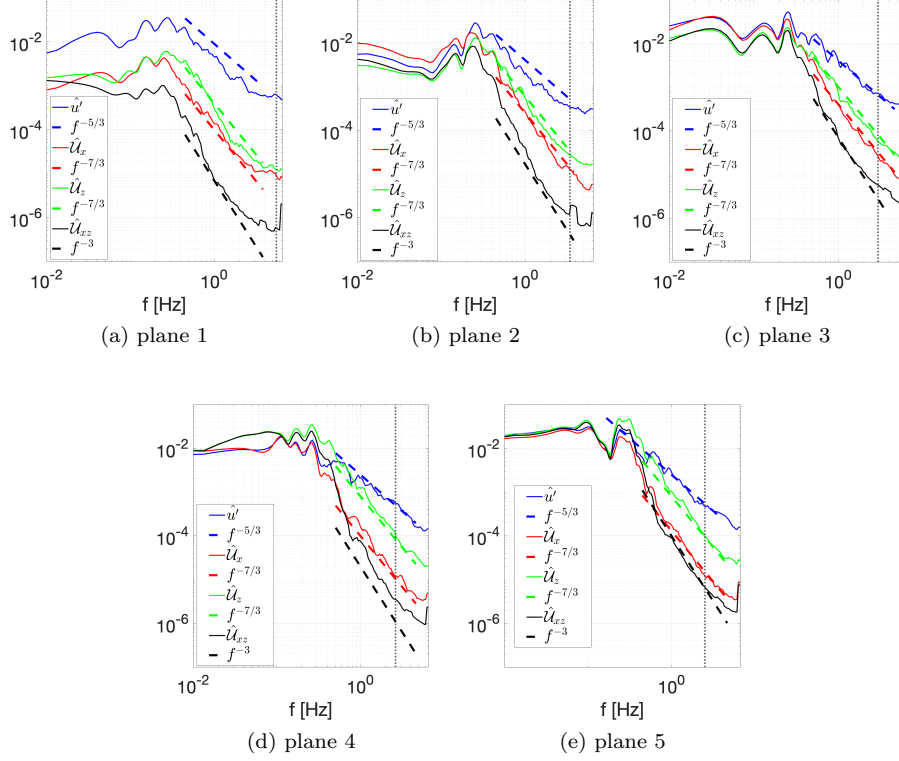
18

Figure 11: Database B: superimposition of PSD computed from one-point velocity sample (blue line), from 1D-spatial averaging velocity either x direction ($\widehat{\mathcal{U}}_x$, red line) or z direction ($\widehat{\mathcal{U}}_z$, green line), and from 2D-spatial averaging velocity ($\widehat{\mathcal{U}}_{xz}$, black line) for several vertical measurement planes (see the location of measurement planes in table 2). Vertical dotted line indicates the frequency corresponding to the integral time-scale.

4.3. Effect on the number of velocity signals on the resulted 1-D integrated velocity spectrum

The spectral analysis is now conducted for the eight flow configurations from database A (four streamwise positions $x^* = [4; 10; 16; 23]$, with and with no turbine) to show the effect of the point number included in the 1D-spatial averaging velocity. First, a representative plot of the PSD computed from the fluctuating streamwise velocity component extracted at one point (with no turbine) is displayed in figure 13a. Each of them exhibits a power law decay proportional to $f^{-5/3}$ which is consistent with the classical Kolmogorov's law Kolmogorov (1991). For the highest frequencies, the PSD remains quite constant showing the experimental noise. This noise is mainly present at $x^* = 4$ and $x^* = 23$ because the corresponding spectra are computed from a point located outside the wake, where the kinetic energy is small. A low frequency signature ($f \simeq 0.3\,\mathrm{Hz}$) of

19

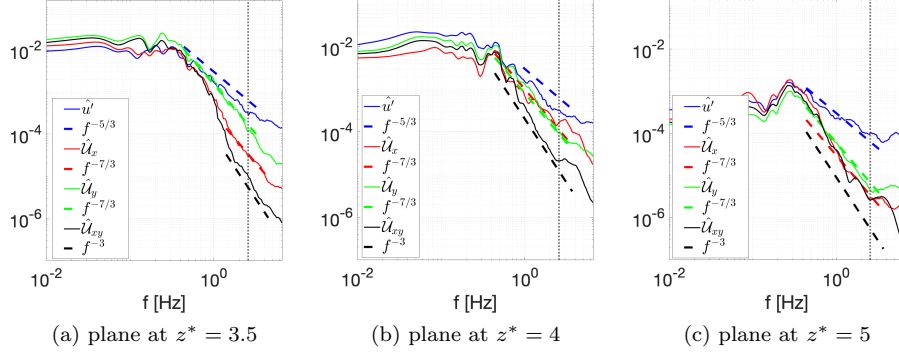(a) plane at $z^* = 3.5$ (b) plane at $z^* = 4$ (c) plane at $z^* = 5$

Figure 12: Database C: superimposition of PSD computed from one-point velocity sample (blue line), from 1D-spatial averaging velocity either x direction ($\widehat{\mathcal{U}}_x$, red line) or y direction ($\widehat{\mathcal{U}}_y$, green line), and from 2D-spatial averaging velocity ($\widehat{\mathcal{U}}_{xy}$, black line) for several horizontal measurement planes. Vertical dotted line indicates the frequency corresponding to the integral time-scale.

the energetic coherent structure is visible for the spectra computed at $x^* = 10$ and $x^* = 16$ because the points are located in the wake of the wall mounted cylinder. Quasi-similar results are observed in presence of the operating turbine as well.
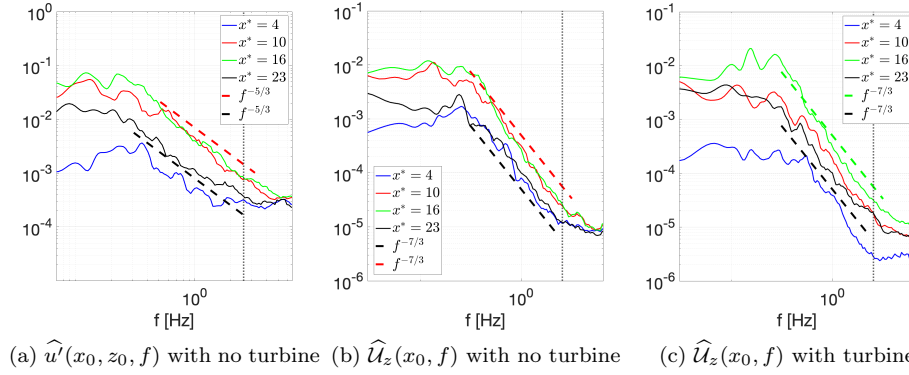

(a) $\widehat{u'}(x_0, z_0, f)$ with no turbine   (b) $\widehat{\mathcal{U}}_z(x_0, f)$ with no turbine   (c) $\widehat{\mathcal{U}}_z(x_0, f)$ with turbine

Figure 13: Database A: a) PSD processed from one-point (x_0, z_0) streamwise velocity component, b) PSD computed from a 1D-spatial averaged velocity along the z-direction with no turbine and c) PSD computed from a 1D-spatial averaged velocity along the z-direction with the operating turbine. In each graph, the four successive rotor locations $x^* = [4; 10; 16; 23]$ are considered. Dashed lines indicate the power law decay. Vertical dotted line indicates the frequency corresponding to the integral time-scale.

Figures 13b and 13c present the PSD of $\mathcal{U}_z$ without and with the turbine respectively. It confirms the previous observation made above (see section 4.2)

20

with a $-7/3$ power-law observed in the inertial range. When PIV measurements
are carried out with no turbine, the mean velocity profile exhibits two main
regions (see figure 5): a uniform flow at the top part and a shear flow in the
bottom. This is different when the operating turbine is present, because of
induction effects which lead to asymmetric mean shear profile from the hub.

Figures 14a, 14b, 14d and 14e compare the PSD processed for $\widehat{\mathcal{U}}_{bottom}$ and
$\widehat{\mathcal{U}}_{top}$ using $N'_z = [34, 54, N_z]$ with and without the operating turbine (green,
black and red curves). To appreciate the convergence better, a one-point velocity
PSD satisfying the Kolmogorov's law (blue curve) and the power law lines ($f^{-5/3}$
and $f^{-7/3}$) are superimposed on each graph. First, it is confirmed that the effect
of the number of Eulerian points on $\widehat{\mathcal{U}}_z$ is found to modify the inertial power law
of the spectrum. The magnitude of the PSD decreases (for $\widehat{\mathcal{U}}_{bottom}$) or increase
(for $\widehat{\mathcal{U}}_{top}$) as the number of points increases. Both $\widehat{\mathcal{U}}_{bottom}$ and $\widehat{\mathcal{U}}_{top}$ spectra
converge towards the $-7/3$ power law in the inertial sub-range. The convergence
to $-7/3$ is observed to be faster in presence of the shear flow. When dealing with
shear profile, local fluctuations at smaller scales are expected to be smoothed
out faster than in presence of uniform velocity profile. In presence of uniform
flow ($\mathcal{U}_{top}$ velocity field), for the smallest values of N'_z (34,54), the associated
spectra $\widehat{\mathcal{U}}_{top}$ exhibit a $-5/3$ power law in the inertial sub-range (figures 14b and
14e). This remark confirms that in the presence of a homogeneous flow field,
a lot of raw velocity signals have to be considered in the spatial averaging to
converge towards the power law of $-7/3$. Paraz and Bandi (2019) estimate that
at least 100 velocity samples have to be added to obtain a converged spectrum
with a power-law of $-7/3$.

Figures 14c and 14f display the spectra $\widehat{\mathcal{U}}_{kdz}$ with $k \in [1, 3, 6, 12, 24, 30]$ and
their corresponding number of Eulerian points $[74, 25, 13, 7, 4, 3]$ respectively.
The case $k = 1$ constitutes the reference spectrum $\widehat{\mathcal{U}}_z(x_0, f)$, already presented
on figures 13b and 13c. The highest spatial discretization is specifically selected
to be smaller than the integral length scale L_x while keeping only three velocity
signals. In this case, the three signals are extracted at $z^* = [2.65, 4.00, 5.35]$ and
the distance between two consecutive Eulerian points is $30dz = 33.6$ mm which is
inferior to $L_x = 0.4$ m (see section 2.2). This remark explains why the frequency
peak related to the energetic dominant flow structure is still present in each
spectrum. To appreciate the convergence better, a one-point velocity spectrum
satisfying the Kolmogorov's law is also superimposed on all graphics. For the
highest frequencies, all PSD remain quite constant. This is a consequence of
the measurement error and of the small scale filtering process as well, which
is induced by the spatial averaging. As k increases, lower eddies are spatially
filtered leading to quite a constant curve observed for the highest frequencies.
But the most remarkable result concerns the power law slope of $-7/3$ that is
obtained for each spectrum $\widehat{\mathcal{U}}_{kdz}$, even in the case of $k = 30$ with only 3 velocity
signals.

Finally, table 4 sums up the different power-laws observed on all spectra of
the spatially averaged velocities, depending on the averaging method. When the
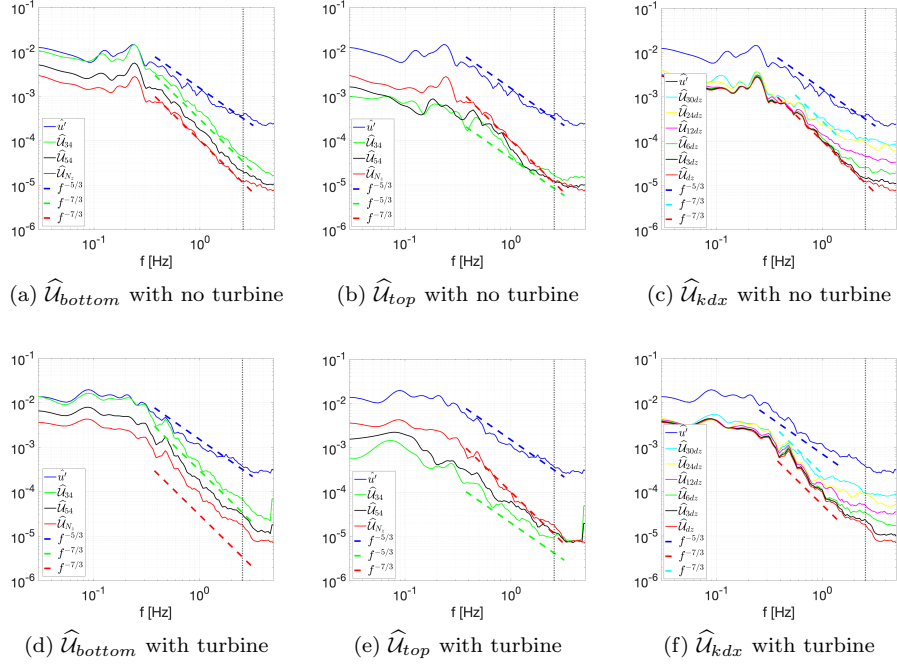
Figure 14: Database A for the location $x^* = 23$ only, with no turbine (top) and with operating turbine (bottom): Superimposition of PSD computed from one-point velocity sample (blue line) and from spatial averaged velocity along the z-direction using various numbers of instantaneous velocity field. a) $\widehat{\mathcal{U}}_{bottom}$ with $N'_z = [34, 54, N_z]$, b) $\widehat{\mathcal{U}}_{top}$ with $N'_z = [34, 54, N_z]$, c) $\widehat{\mathcal{U}}_{kdz}$ with $k \in [1, 3, 6, 12, 24, 30]$. Vertical dotted line indicates the frequency corresponding to the integral time-scale.

velocity is extracted from a single point, the power-law classically corresponds to the -5/3 energy cascade. As soon as the averaging method is 1D, most of the power-law increases and reaches -7/3. This power-law increases again for a 2D averaging method and spectra show a -9/3 power-law characteristic in the inertial range. In the next section, we try to understand and explain the main reasons of these power-law variations.

5. Discussion

Previous results are firstly commented and compared to previous published results. Secondly, since no theoretical explanation is available for this deviation from the classical Kolmogorov law, we investigate the inter-scale coupling by regarding the time correlation of the average velocity field. Thirdly, a direct interpretation of the behaviour of the turbine power spectra is provided based on these previous results.

spatial averaging method	database	spectra power-law in the inertial range
1 point	B & C	-5/3
1 point	A	-5/3
1D	B & C	-7/3*
1D with $iz = 1$ to N_z	A	-7/3
1D with $iz = k\mathrm{d}z$ and $k \leq 30$	A	-7/3
2D	B & C	-9/3

Table 4: Main power-law observed in the inertial frequency range of the spectra processed from the spatially averaged velocities, depending on the averaging method. * In the case of an homogeneous flow direction, the power law is dependent on the number of velocity signals taken into account in the spatial averaging process. A small number leads to a power law of $-5/3$.

5.1. Spatial averaging effect onto velocity spectrum

A first main interesting result to note is that whatever the nature of the flow direction (shear, homogeneity), the spectrum of the 1D-spatially averaged velocity field converges towards a spectrum with a similar power law decay in the inertial range proportional to $f^{-7/3} = f^{-5/3-2/3}$. This is in accordance with previous works (Katzenstein et al., 2010; Bandi, 2017; Paraz and Bandi, 2019) dealing with homogeneous isotropic turbulence signals.

In high-Reynolds number turbulent flows, possibly inhomogeneous and anisotropic, the Kolmogorov's theory asserts that the motion of the smaller eddies (located in the inertial range) is locally isotropic and depends only on the energy containing large scale flow structures and the dissipation rate. This theory of the energy cascade enables some energy transfer mechanisms to be derived in the inertial range like the power law decay proportional to $-5/3$ in the velocity spectrum in this equilibrium range. This Kolmogorov theory of local isotropy means that all high-Reynolds number turbulent flows share some common smaller eddies which slightly contribute to the total flow energy. Consequently, when performing at least 1D or 2D spatial average on a velocity field, this local isotropy is broken. Smaller eddies are filtered away by the spatial averaging and can not satisfy the Kolmogorov's assertion. Even if the present flow organization differs as a function of the direction (shear, homogeneity, etc.), 1D spatial average furthermore leads to the same filtering process in the velocity spectrum inertial range, with an energy decay following a $f^{-7/3}$ power slope. By comparison with the initial one-point Kolmogorov's velocity spectrum, the attenuation of energy occurs over a range of frequencies not necessarily smaller than the associated filter size (spatial discretization). The main difference between the nature of the flow direction concerns the convergence. For a higher shear flow direction, the convergence of the spectral inertial slope is faster than the one obtained from an average over a homogeneous flow direction.

When considering a 2D spatial average, we show that the resulted spectra have a scaling factor of -3 power law decay. Thus, a 2D spatial average can be

23

viewed as a double 1D-spatial average meaning that the second spatial average is applied to a velocity field satisfying a power law decay of $-7/3$ in the inertial range, which differs from the local isotropic turbulence reference. The smoothing effect of the inertial range corresponds then to a similar energetic filtering of the small flow scales which is mathematically translated by an additional power law decay of $-2/3$ in the resulted spectra. The power law decay of -3 can be viewed as $-5/3 - 2 \times 2/3$ when 2 indicates the number of directions along which the spatial average is calculated.

Such a result looks like some previously observed results. Indeed, Amir et al. (2014) have experimentally determined the lift and drag forces acting on sediment particles in a turbulent open-channel flow. Both drag and lift fluctuations have been accessed by spatially averaged drag and lift signals. Starting from the wall pressure exhibiting a $f^{-7/3}$ power law spectrum, they observed that the frequency spectra of both drag and lift fluctuations follow a power law scaling proportional to $-11/3$, where $-11/3 = -7/3 - 2 \times 2/3$. This slope results indeed from an integration along two directions with turbulence-shear interactions. This is recently and numerically confirmed by Ghodke and Apte (2018) in a similar flow configuration.

5.2. Inter-scale coupling analysis

The velocity signal $\mathcal{U}$ is composed of velocity signals spatially distributed in space but sampled at the same frequency. The Wiener-Kinchin theorem enables a direct link to be established between the velocity power spectral density and the velocity autocorrelation. It states that the velocity PSD is the Fourier transform of the velocity autocorrelation. To elucidate the inter-scale coupling, the following two-point autocorrelation tensor is determined, by correlating time-delayed $\widehat{\mathcal{U}}$ signal:

$$
\begin{aligned}
R_{\mathcal{U}\mathcal{U}}(\tau) &= \overline{\mathcal{U}(t)\mathcal{U}(t+\tau)} \\
&= \sum_{i=1}^{N_p} \overline{U_i(t)U_i(t+\tau)} + \sum_{i=1}^{N_p}\sum_{j=1,j\neq i}^{N_p} \overline{U_i(t)U_j(t+\tau)} \qquad (25) \\
&= R_{sc} + R_{cc}
\end{aligned}
$$

where an overbar is the time averaging operator. The first term denoted R_{sc} corresponds to the self correlation and the second term R_{cc} is the cross correlation between temporal signals obtained from the ith and the jth locations. N_p the total number of Eulerian points is equal to N_x, N_y or N_y when dealing with 1D spatial average and to $N_x \times N_y$ or $N_x \times N_z$ for 2D-spatial averaging.

First the two-point correlation tensor and its associated spectrum are analyzed from the following 1D-spatial averaged velocity field: $\mathcal{U}_x$, $\mathcal{U}_z$ and $\mathcal{U}_y$. Based on the two available 2D PIV measurement databases (having the same spatial discretization, see table 1), some illustrative time correlations are presented in figure 15 using $N_p = (99, 36, 74)$ respectively. The large scale energetic structures dictate the two-point correlation $R_{\mathcal{U}\mathcal{U}}$ of the average velocity field. This is more marked when the spatial average is carried out along either the x

or z direction. The 1D-spatial average has very little effect on the large flow scale which remains correlated over time scales. The inter-scale analysis comes from examining the self and cross-correlations which are also plotted for comparison. Whatever the spatial average direction, the self and cross-correlation terms exhibit similar behaviour. The cross-correlation shows however a smaller amplitude than the self correlation, especially when dealing with the main shear z-direction. The shear flow accentuates the dynamic process of small scale smoothing. In each case, a similar spatial discretization was chosen. This emphasizes that the temporal fluctuations over time scales corresponding to all eddies decorrelate faster in presence of a shear flow direction. The smoothing process of shear-direction spatial average is greatly increased by the inter-scale exchange dynamics.
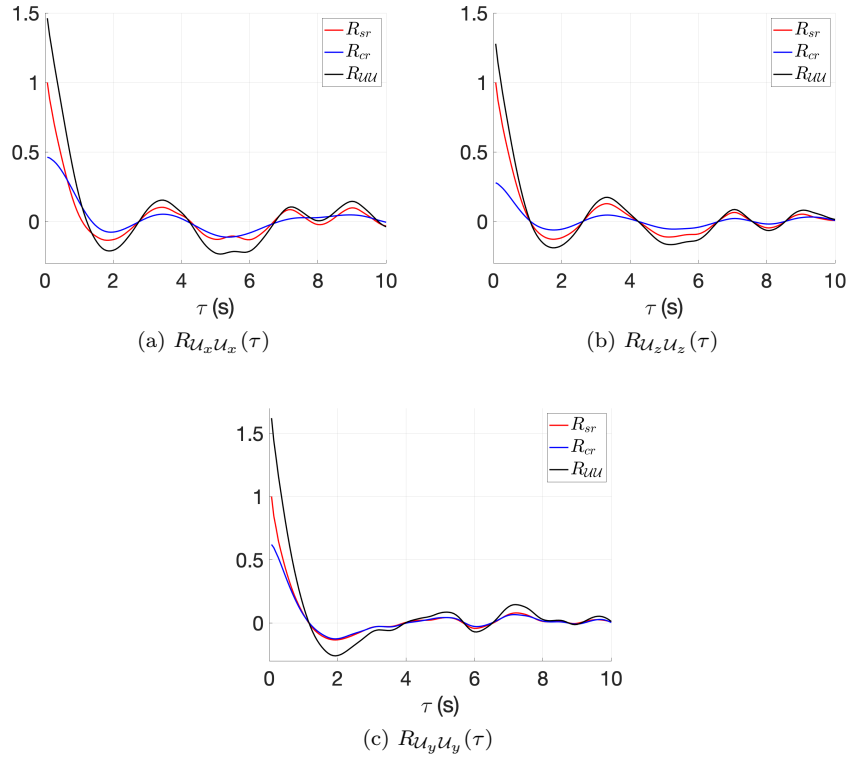

(a) $R_{\mathcal{U}_x \mathcal{U}_x}(\tau)$

(b) $R_{\mathcal{U}_z \mathcal{U}_z}(\tau)$

(c) $R_{\mathcal{U}_y \mathcal{U}_y}(\tau)$

Figure 15: Two-point time correlation computed from 1D-spatial averaged velocity field along x, z and y directions.

The PSD of each two-points correlation ($\widehat{R}_{\mathcal{U}_x \mathcal{U}_x}$, $\widehat{R}_{\mathcal{U}_z \mathcal{U}_z}$ and $\widehat{R}_{\mathcal{U}_y \mathcal{U}_y}$) are now computed and displayed on figures 16. The associated self and cross-correlation PSD are also superimposed on each graph. Even if the spectrum amplitude differs as a function of the self or cross-correlation under consideration, all spectra

25

exhibit a similar power law scaling of $-7/3$ in the inertial range. Thus, the local averaging (R_{sc} term) as well as the non-local averaging (R_{cc} term) leads to a similar scale filtering action in the spectral inertial range. When a 1D-spatial average is processed with a sufficient number of Eulerian points, it seems that a convergence state is reached for both R_{sc} and R_{cc} terms. This underlines that the local isotropy is broken not only by the inter-scale average process between the ith and the jth Eulerian points, but also by the spatial average of the self-correlation over all i^{th} Eulerian points.
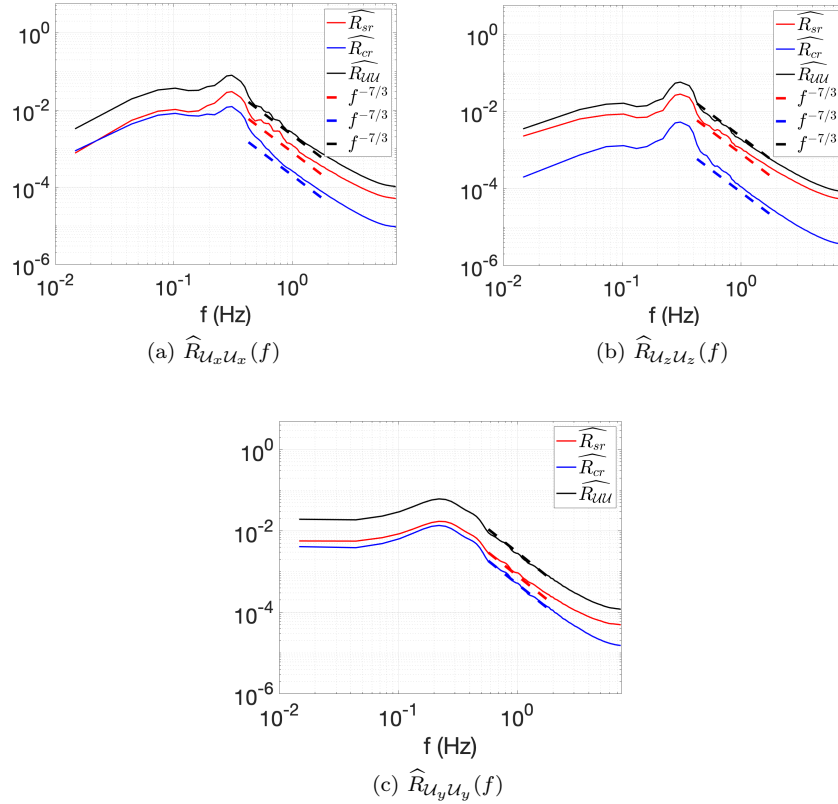

Figure 16: PSD of the two-points time correlation computed from 1D-spatial averaged velocity field, along x, z and y directions.

As done before in section 4.3, instantaneous PIV streamwise velocity components measured along the shear z-direction and in front of an operating turbine (database A) are now used to study the effect of the number of points taken in the average process onto the inter-scale coupling. Using the same notation than before, the two-points correlation, $R_{\mathcal{U}_{kdz}\mathcal{U}_{kdz}}(\tau)$ is determined with $k \in [6, 12, 30]$, leading to $N_p \in [13, 7, 3]$ respectively. A comparison of the two-

points correlation and its self and cross-correlation counterparts is done and
presented on figure 17. As the spatial discretizations between reference Eulerian
points are always smaller than the integral scale of the flow, the energy contain-
ing eddies are well recovered especially in the self-correlation term. Moreover,
the amplitude of R_{sc} decreases rapidly as τ increases. This is mainly true when
only 3 reference Eulerian points are kept in the spatial averaged velocity field,
$\mathcal{U}_{30\mathrm{dz}}$. The R_{cc} term is of very small amplitude, mainly in the $R_{\mathcal{U}_{30\mathrm{dz}}\mathcal{U}_{30\mathrm{dz}}}(\tau)$
correlation. For a larger time lag however, the amplitude of R_{cc} terms is slightly
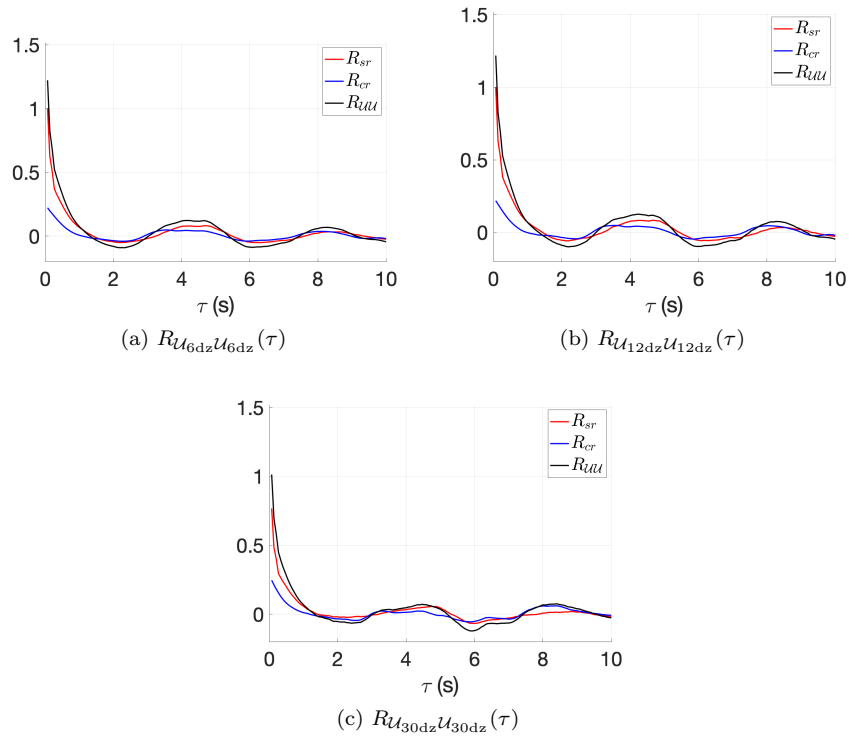higher than the R_{sc} term.

(a) $R_{\mathcal{U}_{6\mathrm{dz}}\mathcal{U}_{6\mathrm{dz}}}(\tau)$

(b) $R_{\mathcal{U}_{12\mathrm{dz}}\mathcal{U}_{12\mathrm{dz}}}(\tau)$

(c) $R_{\mathcal{U}_{30\mathrm{dz}}\mathcal{U}_{30\mathrm{dz}}}(\tau)$

Figure 17: Two-points time correlation computed from $\mathcal{U}_{k\mathrm{dz}}(t)$ with a step $k$dz and $k \in$
$[6, 12, 30]$ corresponding to $N_p \in [13, 7, 3]$.

Figure 18 displays the corresponding PSD. Whatever the case, $\widehat{R_{sc}}$ exhibits
a power law scaling of $-5/3$ in the inertial range, while the other $\widehat{R_{\mathcal{U}\mathcal{U}}}$ and $\widehat{R_{cc}}$
spectra have a scaling of $-7/3$. This demonstrates that when a small number of
Eulerian points is retained in $\mathcal{U}$, the spectrum of the cross-correlation between
the ith and the jth Eulerian points always presents a $-7/3$ power law which has
been found on the whole correlation spectrum $\widehat{R_{\mathcal{U}\mathcal{U}}}$. When considering a very
small number of Eulerian points, the ith and j^{th} Eulerian points are separated
by a large distance. Then temporal fluctuations over time scales corresponding

27

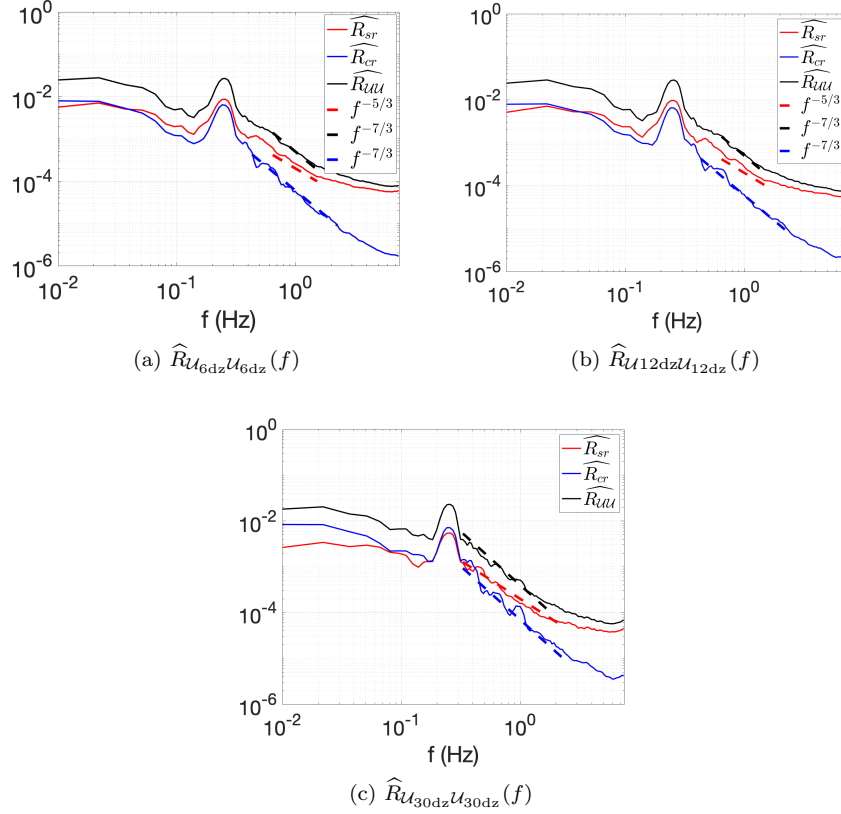to all flow structures of size smaller than this distance decorrelate.

(a) $\widehat{R}_{\mathcal{U}_{6\mathrm{dz}}\mathcal{U}_{6\mathrm{dz}}}(f)$

(b) $\widehat{R}_{\mathcal{U}_{12\mathrm{dz}}\mathcal{U}_{12\mathrm{dz}}}(f)$

(c) $\widehat{R}_{\mathcal{U}_{30\mathrm{dz}}\mathcal{U}_{30\mathrm{dz}}}(f)$

Figure 18: PSD of the two-points time correlation computed from $\mathcal{U}_{k\mathrm{dz}}(t)$ with a step $k\mathrm{dz}$ and $k \in [6, 12, 30]$ corresponding to $N_p \in [13, 7, 3]$.

5.3. Turbine power and thrust spectra

In section 3.2, turbine power and thrust fluctuations are found to be linearly dependent on the spatially averaged velocity field. If the disk average hypothesis is used, the turbine power and thrust spectra are similar to a 2D spatial integration of the velocity field, which finally corresponds to a 2D spatial averaged velocity field. Yet, turbine thrust and torque spectra exhibit a power law decay of $-11/3$ (figure 8) which differs from 2D spatial average velocity spectra showing a power law decay of -3. Equation 15 is then considered taking into account the local force related to each blade. The total thrust force is then obtained by summing these three contributions as follows:

$$\mathcal{F}(t) = \sum_{i=1}^{3} F_{xi}(t) \tag{26}$$

28

As the fluctuations of the blade force contributing to the thrust F_{xi} are also measured separately (see 2.1), the total thrust spectrum of the turbine is then:

$$\widehat{\mathcal{F}}(f) = \widehat{\sum_{i=1}^{3} F_{xi}}(f) \tag{27}$$

The PSD representation of $\widehat{\mathcal{F}}$ is given in figure 19 which is quasi-similar to the PSD of $\widehat{T}$ presented on figure 8. The magnitude is only reduced because of the additional hub load contribution in the global thrust measurement. The main frequency peak is located at $f = 5.4\,\mathrm{Hz}$ which corresponds to the blade passing frequency and the second frequency peak $f \simeq 10\,\mathrm{Hz}$ is its first sub-harmonic. The inertial range also shows an energy decay with a $f^{-11/3}$ power law. On figure 19b, for each streamwise position, PSD of the fluctuations of a single blade force $\widehat{F}_{x1}(f)$ are plotted (blade 1). Similar representations are obtained for the two other blade force fluctuations ($i = 2, 3$). A power law decay proportional to -3 is observed in the inertial sub-range. Such a scaling effect is directly linked to the 2D-spatial average of the velocity field over the blade surface (equation 7). A direct physical interpretation of the power law decay of the single-blade load spectrum is then accessed. The total turbine thurst (or power) signal can then be viewed as the summation of 3 distinct signals. Each one has a spectrum power decay of -3 in the inertial frequency range. By performing an ensemble average over the 3 blades, a smoothing process is then observed in the inertial range that can be identical to the one obtained when dealing with an inhomogeneous shear flow field. In this case, it was previously demonstrated that the spatial average effect on the velocity spectrum is increased. The resulted spectrum converges towards an additional power law decay of $-2/3$ in the inertial range, even in the presence of a fairly reduced number of velocity field (see §4.3, with only 3 velocity fields). Note that when considering the blade drag force signals, the convergence towards an additional power law decay of -2/3 is reinforced due to the motion of the blades enhancing the signal non-homogeneity. In this sense, the observed power law decay of $-11/3$ in the total thrust force is interpreted as an effect of a 2D spatial averaging of velocity field and an ensemble average over the three blades. Similar considerations can be made to physically interpret the $-11/3$ scaling in the turbine power spectrum.

Previous developments allow a direct interpretation of the turbine power spectra with the energy decaying as $f^{-11/3}$. This approach relies on applying a low pass filtering process between incoming turbulence and the turbine power. This can be related to previous works by Tobin et al. (2015); Chamorro et al. (2015b); Liu et al. (2017) where a transfer function $G(f) = f^{-2}$ has been proposed to link the incoming velocity spectra to turbine power. This transfer function can then be physically interpreted as a consequence of a 2D-spatial averaged velocity field coupled with the power and thrust average over the blades.

6. Conclusion

To reproduce a realistic turbulent flow that can impact a turbine, the 3D wake flow developing behind a wall-mounted cylinder has been considered. Such
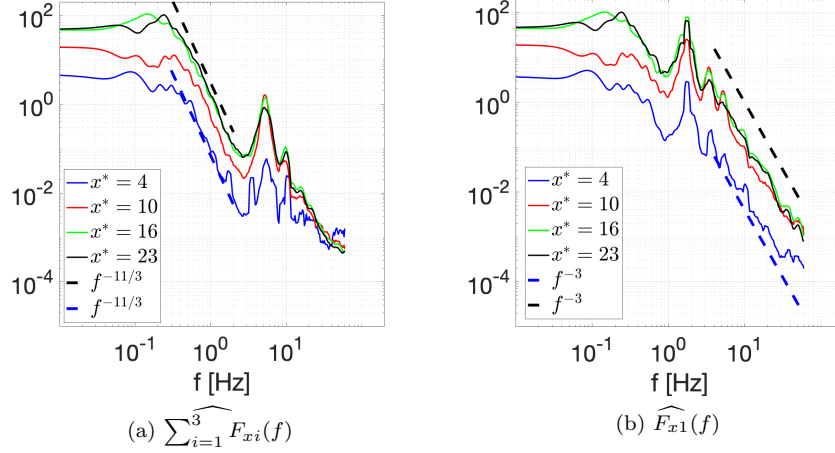
Figure 19: a) Total thrust PSD of the turbine for the four successive rotor locations $x^* = [4; 10; 16; 23]$. b) PSD of one single blade force F_{x1}, for the four rotor locations.

a high-Reynolds number turbulent flow is inhomogeneous with a high vertical mean-shear velocity profile. It is representative of a turbulent flow that could interact with a tidal turbine as well as a wind turbine. A 1:20 horizontal-axis turbine model has been positioned at different streamwise locations in this turbulent shear flow, in order to elucidate the interaction between incoming flow properties and the turbine performance. This is of great importance for the turbine operational life, especially in terms of device and material fatigue, maintenance costs and integration with the electricity grid.

The measurement of the turbine thrust and torque momentum have confirmed that their spectra exhibit a power law decay proportional to $-11/3$ in the inertial range. After analytically determining the expression of turbine thrust force and torque momentum, it is demonstrated that these quantities are linearly dependent on the spatial integrated (or averaged) velocity field impacting the rotor turbine. Based on planar PIV velocity measurements, we then analyzed the effect of the velocity spatial average on its resulted spectrum. Even if the PIV sampling frequency as well as the spatial discretization are not sufficient to entirely investigate the whole inertial range of the velocity spectrum, the main part of the inertial range is covered, enabling such an investigation.

The 1D-spatial average has been conducted along each separate direction. Such spatial averaging induces a small scales filter leading to an attenuation of the spectral slope in the inertial range. It was observed that the resulted PSD exhibits a power law decay of $-7/3$ in the sub-range, whatever the flow direction along with the average carried out, when a sufficient number of velocity signals is considered. However, the convergence towards this $-7/3$ scaling is accelerated

30

in presence of the shear flow direction. In this last case, a very reduced number of velocity signals is enough to achieve convergence.

Applying a 2D-spatial average before computing the velocity spectrum implies an additional smoothing effect of smaller scales and then an energy decay as f^{-3} in the spectral inertial range. This makes us to speculate that in a 3D high-Reynolds number inhomogeneous turbulent flow, satisfying local Kolmogorov's power law decay, the velocity spectrum of its spatial average along N direction(s) has an inertial slope of $-5/3 - N \times 2/3$.

An analysis of the inter-scale coupling effect was performed thanks to the two-points correlation of the average velocity field. It is especially observed that in presence of a small number of Eulerian points, the spectral content of this correlation is imposed by the cross-correlation term. It means that the energy filtering process operates from Eulerian points which are separated by a large distance.

Finally, this information is used to interpret the inertial range power-law exponents of the turbine load and power spectra. The $-11/3$ scaling results from a 2D-spatial averaged velocity field coupled with the thrust and power average over the blades. To explain this scaling, previous studies have proposed a transfer function corresponding to a low pass filtering process between incoming turbulence and the turbine power. In the present work, the physical origin of this scaling is then accessed. Present results allows then a better physical interpretation of the turbine power variabilities related to temporal fine-scale fluctuations and could be used to improve the integration of the tidal or wind turbines into the electricity grid (Lewis et al., 2019). As a future work, other kinds of tidal flow including turbulent and wake turbine induced flows (Allmark et al., 2021; Ebdon et al., 2021) could be analyzed to confirm the effect of spatial averaging on the resulting turbine power spectra. More specifically, when regarding the turbulent and wake flows around a turbine, the integral flow length-scale can reach one rotor diameter (Ebdon et al., 2021) or higher. The effect of flow integral length-scales on the small scale filtering process has then to be clarified, especially in comparison to the rotor diameter. Moreover, some numerical simulations could be performed to access numerical velocity signals with a better time resolution as well as spatial resolution. That would enable the spectral slope behaviour in the whole inertial range to be to confirmed and entirely validated.

Acknowledgements

thank Thomas Bacchetti and Jean-Valery Facq for their assistance and precious advices.

CRediT authorship contribution statement

References

Ahmed, U., Apsley, D., Afgan, I., Stallard, T., Stansby, P., 2017. Fluctuating loads on a tidal turbine due to velocity shear and turbulence: Comparison of CFD with field data. Renewable Energy 112, 235–246.

Allmark, M., Ellis, R., Ebdon, T., Lloyd, C., Ordonez-Sanchez, S., Martinez, R., Mason-Jones, A., Johnstone, C., O'Doherty, T., 2021. A detailed study of tidal turbine power production and dynamic loading under grid generated turbulence and turbine wake operation. Renewable Energy 169 169, 1422–1439.

Amir, M., Nikora, V. I., Stewart, M. T., 2014. Pressure forces on sediment particles in turbulent open-channel flow: A laboratory study. Journal of Fluid Mechanics 757, 458–497.

Apt, J., 2007. The spectrum of power from wind turbines. Journal of Power Sources 169 (2), 369–374.

Bahaj, A. S., Molland, A. F., Chaplin, J. R., Batten, W. M. J., 2007. Power and thrust measurements of marine current turbines under various hydrodynamic flow conditions in a cavitation tunnel and a towing tank. Renewable Energy 32 (3), 407–426.

Baidya, R., Philip, J., Hutchins, N., Monty, J. P., Marusic, I., 2019. Spatial averaging effects on the streamwise and wall-normal velocity measurements in a wall-bounded turbulence using a cross-wire probe. Measurement Science and Technology 30 (8).

Bandi, M. M., 2017. Spectrum of Wind Power Fluctuations. Physical Review Letters 118 (2), 1–5.

Bartl, J., Sætran, L., 2017. Blind test comparison of the performance and wake flow between two in-line wind turbines exposed to different turbulent inflow conditions. Wind Energy Science 2 (1), 55–76.

Blackmore, T., Myers, L. E., Bahaj, A. S., 2016. Effects of turbulence on tidal turbines: Implications to performance, blade loads, and condition monitoring. International Journal of Marine Energy 14, 1–26.

32

Bossuyt, J., Meneveau, C., Meyers, J., 2017. Wind farm power fluctuations and spatial sampling of turbulent boundary layers. Journal of Fluid Mechanics 823, 329–344.

Chamorro, L. P., Hill, C., Morton, S., Ellis, C., Arndt, R. E. A., Sotiropoulos, F., 2013. On the interaction between a turbulent open channel flow and an axial-flow turbine. Journal of Fluid Mechanics 716, 658–670.

Chamorro, L. P., Hill, C., Neary, V. S., Gunawan, B., Arndt, R. E., Sotiropoulos, F., 2015a. Effects of energetic coherent motions on the power and wake of an axial-flow turbine. Physics of Fluids 27 (5), 1–12.

Chamorro, L. P., Hill, C., Neary, V. S., Gunawan, B., Arndt, R. E. A., Sotiropoulos, F., 2015b. Effects of energetic coherent motions on the power and wake of an axial-flow turbine. Physics of Fluids 27 (5).

Chamorro, L. P., Lee, S.-J., Olsen, D., Milliren, C., Marr, J., Arndt, R., Sotiropoulos, F., 2015c. Turbulence effects on a full-scale 2.5 MW horizontal-axis wind turbine under neutrally stratified conditions. Wind Energy 18 (2), 339–349.

Churchfield, M. J., Lee, S., Michalakes, J., Moriarty, P. J., 2012. A numerical study of the effects of atmospheric and wake turbulence on wind turbine dynamics. Journal of Turbulence 13 (May), 1–32.

Deskos, G., Payne, G. S., Gaurier, B., Graham, M., 2020. On the spectral behaviour of the turbulence-driven power fluctuations of horizontal-axis turbines. Journal of Fluid Mechanics 904, A13.

Durán Medina, O., Schmitt, F. G., Calif, R., Germain, G., Gaurier, B., 2017. Turbulence analysis and multiscale correlations between synchronized flow velocity and marine turbine power production. Renewable Energy 112, 314–327.

Ebdon, T., Allmark, M. J., O'Doherty, D. M., Mason-Jones, A., O'Doherty, T., Germain, G., Gaurier, B., 2021. The impact of turbulence and turbine operating condition on the wakes of tidal turbines. Renewable Energy 165, 96–116.

Foucaut, J. M., Carlier, J., Stanislas, M., 2004. PIV optimization for the study of turbulent flow using spectral analysis. Measurement Science and Technology 15 (6), 1046–1058.

Gaurier, B., Druault, P., Ikhennicheu, M., Germain, G., 2020a. Experimental analysis of the shear flow effect on tidal turbine blade root force from three-dimensional mean flow reconstruction. Phil. Trans. R. Soc. A. 378 (20200001).

Gaurier, B., Germain, G., Facq, J.-V., Bacchetti, T., 2018. Wave and current flume tank of IFREMER at Boulogne-sur-mer. Description of the facility and its equipment. Tech. rep., Ifremer.

Gaurier, B., Germain, G., Facq, J.-V., Johnstone, C., Grant, A. D., Day, A. H., Nixon, E., Di Felice, F., Costanzo, M., 2015. Tidal energy "round Robin" tests comparisons between towing tank and circulating tank results. International Journal of Marine Energy 12, 87–109.

Gaurier, B., Ikhennicheu, M., Germain, G., Druault, P., 2020b. Experimental study of bathymetry generated turbulence on tidal turbine behaviour. Renewable Energy 156, 1158–1170.

Gayme, D. F., Chakrabortty, A., 2012. Impact of wind farm placement on inter-area oscillations in large power systems. In: 2012 American Control Conference (ACC). IEEE, pp. 3038–3043.

Ghodke, C. D., Apte, S. V., 2018. Spatio-temporal analysis of hydrodynamic forces on the particle bed in an oscillatory flow environment. Journal of Fluid Mechanics 841, 167–202.

Hackett, E. E., Luznik, L., Katz, J., Osborn, T. R., 2009. Effect of finite spatial resolution on the turbulent energy spectrum measured in the coastal ocean bottom boundary layer. Journal of Atmospheric and Oceanic Technology 26 (12), 2610–2625.

Ikhennicheu, M., 2019. Étude expérimentale de la turbulence dans les zones à forts courants et de son impact sur les hydroliennes. Ph.D. thesis, Université de Lille.

Ikhennicheu, M., Druault, P., Gaurier, B., Germain, G., 2020. Turbulent kinetic energy budget in a wall-mounted cylinder wake using PIV measurements. Ocean Engineering 210 (May), 107582.

Ikhennicheu, M., Germain, G., Druault, P., Gaurier, B., 2019a. Experimental investigation of the turbulent wake past real seabed elements for velocity variations characterization in the water column. International Journal of Heat and Fluid Flow 78, 108426.

Ikhennicheu, M., Germain, G., Druault, P., Gaurier, B., 2019b. Experimental study of coherent flow structures past a wall-mounted square cylinder. Ocean Engineering 182, 137–146.

Jin, Y., Ji, S., Chamorro, L. P., 2016. Spectral energy cascade of body rotations and oscillations under turbulence. Physical Review E 94 (6), 063105.

Katzenstein, W., Fertig, E., Apt, J., 2010. The variability of interconnected wind plants. Energy Policy 38 (8), 4400–4410.

Kolmogorov, A. N., 1991. The local structure of turbulence in incompressible viscous fluid for very large Reynolds numbers. Proceedings of the Royal Society of London. Series A: Mathematical and Physical Sciences 434 (1890), 9–13.

Lavoie, P., Avallone, G., De Gregorio, F., Romano, G. P., Antonia, R. A., 2007. Spatial resolution of PIV for the measurement of turbulence. Experiments in Fluids 43 (1), 39–51.

Lewis, M., McNaughton, J., Marquez-Dominguez, C., Todeschini, G., Togneri, M., Masters, I., Allmark, M., Stallard, T., Neill, S., Goward-Brown, A., Robins, P., 2019. Power variability of tidal-stream energy and implications for electricity supply. Energy 183, 1061–1074.

Li, Q., Murata, J., Endo, M., Maeda, T., Kamada, Y., 2016. Experimental and numerical investigation of the effect of turbulent inflow on a Horizontal Axis Wind Turbine (Part I: Power performance). Energy 113, 713–722.

Liu, H., Jin, Y., Tobin, N., Chamorro, L. P., 2017. Towards uncovering the structure of power fluctuations of wind farms. Physical Review E 96 (6), 3–8.

Magnier, M., Druault, P., Gaurier, B., Germain, G., 2020. Comparison of bathymetry variation effects on tidal turbine behaviour. In: 17èmes journées de l'hydrodynamique. Cherbourg, France.

Mycek, P., Gaurier, B., Germain, G., Pinon, G., Rivoalen, E., 2014. Experimental study of the turbulence intensity effects on marine current turbines behaviour. Part I: One single turbine. Renewable Energy 66, 729–746.

Paraz, F., Bandi, M. M., 2019. Second order structure functions for higher powers of turbulent velocity. Journal of Physics Condensed Matter 31 (48).

Payne, G. S., Stallard, T., Martinez, R., Bruce, T., 2018. Variation of loads on a three-bladed horizontal axis tidal turbine with frequency and blade position. Journal of Fluids and Structures 83 (2018), 156–170.

Sentchev, A., Thiébaut, M., Schmitt, F., 2020. Impact of turbulence on power production by a free-stream tidal turbine in real sea conditions. Renewable Energy 147 (1), 1932–1940.

Sjöholm, M., Mikkelsen, T., Kristensen, L., Mann, J., Kirkegaard, P., 2010. Spectral analysis of wind turbulence measured by a Doppler Lidar for velocity fine structure and coherence studies. In: 15th International Symposium for the Advancement of Boundary Layer Remote Sensing (ISARS). Palaiseau, France.

Thiébaut, M., Filipot1, J., Maisondieu, C., Damblans, G., Jochum, C., Kilcher, L., Guillou, S., 2020. Characterization of the vertical evolution of the three-dimensional turbulence for fatigue design of tidal turbines. Phil. Trans. R. Soc. A: 378 (20190495).

Tobin, N., Zhu, H., Chamorro, L. P., 2015. Spectral behaviour of the turbulence-driven power fluctuations of wind turbines. Journal of Turbulence 16 (9), 832–846.

900   Wagner, R., Antoniou, I., Pedersen, S. M., Courtney, M. S., Jørgensen, H. E., 2009. The influence of the wind speed profile on wind turbine performance measurements. Wind Energy 12 (4), 348–362.

Wyngaard, J. C., 1968. Measurement of small-scale turbulence structure with hot wires. Journal of Physics E: Scientific Instruments 1 (11), 1105–1108.